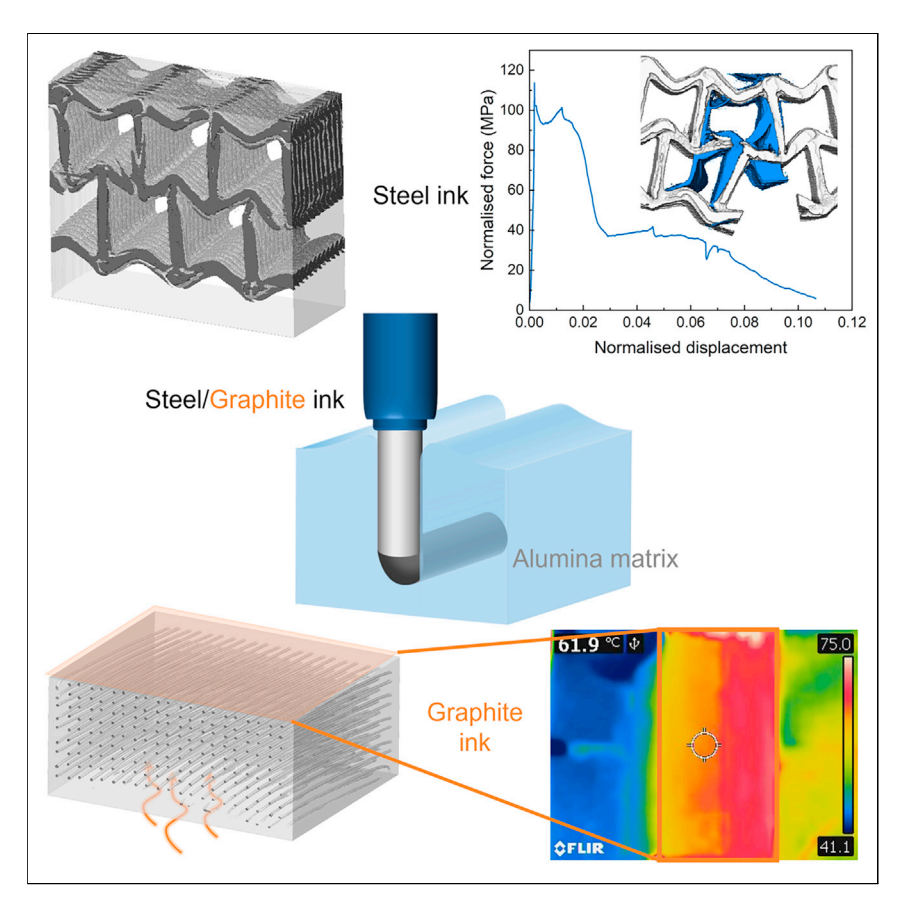
# **Matter**



### **Article**

# Embedded 3D printing of microstructured multi-material composites



The AM of ceramic composites with accurate microstructural control is challenging due to the lack of appropriate techniques and the difficulty in postprocessing. Here, we tackle this challenge using a simple, one-step approach for the embedded 3D printing of complex, fine structures inside dense ceramics. This approach enables the production of multi-material parts with refined structural manipulation and opens new opportunities for the design and fabrication of composites.

Shitong Zhou, Iuliia S.
Tirichenko, Xun Zhang, ..., Philip
J. Withers, Florian Bouville,
Eduardo Saiz

s.zhou18@imperial.ac.uk (S.Z.) e.saiz@imperial.ac.uk (E.S.)

#### Highlights

3D printing of multi-material inorganic composites with refined microstructural control

Introduction of auxetic reinforcement structures in ceramics to maximize fracture energy

Fabrication of 3D microchannel arrays in refractory ceramics for thermal management



Zhou et al., Matter 7, 668–684 February 7, 2024 © 2023 The Authors. Published by Elsevier Inc.

https://doi.org/10.1016/j.matt.2023.10.031







#### Article

# Embedded 3D printing of microstructured multi-material composites

Shitong Zhou,<sup>1,3,\*</sup> Iuliia S. Tirichenko,<sup>1</sup> Xun Zhang,<sup>2</sup> Yinglun Hong,<sup>1</sup> Harry Payne,<sup>1</sup> Philip J. Withers,<sup>2</sup> Florian Bouville,<sup>1</sup> and Eduardo Saiz<sup>1,\*</sup>

#### **SUMMARY**

Additive manufacturing could open new opportunities in the design of advanced composites and multi-material devices. However, when it comes to the combination of inorganic materials, it is difficult to achieve the structural control demanded by many advanced applications. To address this challenge, we have formulated a self-healing ceramic gel that enables the movement of a printing nozzle in its interior. After a heat treatment, the gel forms a defect-free ceramic encapsulating the printed structure. We have used this technique to print sacrificial lightweight graphite structures as well as dense steel frameworks within an alumina ceramic. The graphite is used to generate complex microchannel arrays, whereas the introduction of auxetic steel structures results in works of fracture 50% greater than those obtained with simple fiber arrays and orders of magnitude above the fracture energy of the matrix. These results suggest that embedded 3D printing can open the way to implement new composite designs.

#### **INTRODUCTION**

The attractive properties of ceramic materials such as high strength, hardness, good thermal stability, and oxidation resistance make them the ideal candidates for many applications, particularly those involving exposure to demanding environments. However, the same properties that make ceramics so appealing render their machining and shaping particularly challenging. <sup>1–4</sup> In addition, high performance demands a reliable control of the material architecture from the nano-level upward and often requires the assembly of several phases. Perhaps nowhere is this more evident than in the need to enhance the fracture resistance of ceramics for highly demanding structural applications. This need has triggered a significant research effort in the field of ceramic composites that goes from the more established methodologies of using fiber and particulate reinforcements to new approaches that look at motifs in natural materials for inspiration. Additive manufacturing could help to answer these challenges by opening up new avenues for the fabrication of ceramic structures and devices with bespoke geometries and unique architectures.

The term "additive manufacturing" (AM) (also known as 3D printing) encompasses a broad set of techniques by which objects are built up layer by layer according to a computer-aided design (CAD). 5–8 These techniques are now applied to a wide range of materials, including metals, ceramics, and polymers. This design flexibility, and the ability to implement hierarchical architectures, make the AM of ceramics particularly interesting. Several AM techniques (binder jetting, selective laser melting, stereolithography, etc.) are currently being investigated for the fabrication of

#### **PROGRESS AND POTENTIAL**

Although 3D printing has the potential to manufacture complex composites and devices at large scale, so far, we have been unable to fully harness this potential. As a result, the structural control attained is often well below the demand of advanced technologies. This work demonstrates the process of embedded printing to integrate complex structures inside dense inorganic materials by fine-tuning the rheology of the printing system and careful postprocessing to form defectfree materials.

Our approach allows the microstructural manipulation of multi-material structures as required in many structural and functional applications from energy storage to transportation. By incorporating refined metamaterial structures in dense ceramics, it opens a path to break the conflict between strength and toughness. Another advantage is the flexibility of the process, which enables printing with a wide range of materials from dense hydrophilic compounds such as steel to light hydrophobic ones like carbon.



# **Matter** Article



ceramic parts.<sup>7,9</sup> Among these, robocasting (also called direct ink writing) is emerging as a very promising, and conceptually simple, method. In robocasting, a green ceramic body is prepared through the continuous extrusion of a ceramic paste (or ink). 10 After printing, the green body is dried, debinded, and sintered to form a dense ceramic. However, the practical application of ceramic AM faces several challenges. One challenge is the need for reliable methodologies for building complex devices and composites combining different materials. Although in direct ink writing this can be achieved by combining more than one printhead or switching feeding systems, the process is not simple, and the range of geometries that can be printed is currently limited. 11

Embedded 3D printing is an emerging variant of robocasting based on the printing of a complex structure inside a soft supporting matrix. 12 It has been successfully used to build vascular networks in hydrogels by printing sacrificial channels, <sup>13,14</sup> to insert sensors in polymers, 15,16 and to fabricate ceramic parts having complex shapes by using the matrix as a sacrificial support that is subsequently eliminated to retrieve the part. 17-25 In these cases, different systems have been used, including wateror oil-based matrices and granular gels (e.g., water with laponite, oil with fumed silica, modified hyaluronic acid, and Carbopol microgels). 17,18,26-28 The rheological behavior of water and oil suspensions depends on the solid loading, and organic granules in the granular gels are larger than the inorganic powders used in processing. Therefore, these gels are not good candidates to formulate printing inks containing inorganic particles, whereas thermally reversible Pluronic hydrogels have been proved to be a suitable carrier for ceramic powders in robocasting. 9,10

Despite the progress reported in the development of embedded printing in organic systems, there are no reports of the use of this technique to build complex structures inside dense inorganic materials. This is because the translation of the technology to inorganic systems is not straightforward. Here, we have developed embedded printing as a way to print complex metallic and carbon structures inside a dense ceramic and show how this technique enables the fabrication of composites incorporating metamaterial reinforcements or the introduction of 3D microchannel arrays in ceramics. The requirements for embedded printing to fabricate dense, defect-free materials in inorganic systems are more stringent than those for printing in polymers or sacrificial supporting gels. The rheological properties of the gels containing high loads of ceramic, carbon, or metallic particles are different, and the postprocessing steps (drying and sintering) are equally important. Our printing inks and the selfhealing matrices are formed by Pluronic gels containing inorganic powders. The matrix should support the weight of the inserted printed parts (which can be significantly denser than a polymer) and heal completely after the printing nozzle has passed. After drying and sintering, it should form a dense, defect-free ceramic that encapsulates the printed structure. In addition, this printed structure should reproduce the design without distortion. To achieve these goals, it is necessary to match the viscoelastic behavior of matrix and ink and to control the post-printing process.

We demonstrate the potential of embedded printing with two distinct examples in aluminum oxide, one in which we use hydrophilic powders (steel) to print a structure that is denser than the matrix and the other where it is less dense (built with hydrophobic graphite). In the first case, we print a range of internal reinforcing framework structures from unidirectional fiber arrays to auxetic, with the aim of increasing the fracture energy. In the second example, the graphite structure is subsequently eliminated to form complex microchannel arrays in alumina and build microfluidic

https://doi.org/10.1016/j.matt.2023.10.031

<sup>&</sup>lt;sup>1</sup>Centre of Advanced Structural Ceramics, Department of Materials, Imperial College London, London SW7 2AZ, UK

<sup>&</sup>lt;sup>2</sup>Henry Royce Institute, Department of Materials, The University of Manchester, Manchester M13 9PL. UK

<sup>3</sup>Lead contact

<sup>\*</sup>Correspondence: s.zhou18@imperial.ac.uk (S.Z.), e.saiz@imperial.ac.uk (E.S.)





devices. Our results suggest that embedded printing could be a viable alternative for the fabrication of a wide range of multi-material structures within a broad design space.

#### **RESULTS AND DISCUSSION**

#### **Embedded printing process optimization**

The embedded printing process is described in Figure 1A and can be visualized in the Supplementary information (Video S1). In our system, both ink and matrix are based on a thermally reversible hydrogel Pluronic F127 containing inorganic powders. Pluronic has a triblock structure comprising hydrophilic polyethylene oxide (PEO) and hydrophobic polypropyleneoxide (PPO) groups in a 2:1 ratio (Figure 1B). <sup>10</sup> At a low temperature, the copolymer groups dissolve in water. Pluronic suspensions undergo gelation above a critical transition temperature accompanied by a three orders of magnitude increase in viscosity, due to micelle formation and hydrophobic association (Figure 1C). <sup>29</sup> The viscosity and the transition temperature are largely defined by the Pluronic concentration and the volume fraction of inorganic powder. <sup>30,31</sup> To warrant the formation of dense/defect-free materials after drying and sintering, the inorganic content of the gels used in the matrix and inks has to be relatively high. All our gels have powder contents above 25 vol %.

At a temperature close to 0°C, the matrix gel exhibits low viscosity and can be cast into a silicone mold in a step akin to the gel casting process often used with technical ceramics.  $^{32-34}$  At this temperature, the suspension can flow easily and fill the mold without trapping air bubbles. Subsequently, the temperature is raised and continuously monitored until it reaches the desired value for printing (Figure 1A). At this point, the printing nozzle is inserted into the gel and is held there for a few seconds until the matrix recovers its stiffness (Figure 1D). Then, the nozzle moves along the pre-programmed path while extruding the ink. Once the printing nozzle has passed, the matrix flows back to heal the gap left by the nozzle, that is the crevice, recovering its strength and stiffness to support the printed structure. Complete matrix healing is required to form a dense, defect-free ceramic after sintering. At the same time, the printed part should not displace or distort under the effects of gravity ( $\overrightarrow{F_g}$ ), buoyancy ( $\overrightarrow{F_b}$ ), or capillary forces. Using this approach, we have built a series of steel and graphite structures inside dense alumina (Figures 1E–1H; CAD models in Figure S1).

The print fidelity and resolution depend on a delicate interplay between the viscoelastic properties of matrix and ink. To meet the requirements, the rheology of a matrix containing 37 vol % Al<sub>2</sub>O<sub>3</sub> in 25 wt % Pluronic gel was manipulated by controlling the printing temperature (Figures 2A and S2). Its behavior can be described using the Herschel-Bulkley equation (Figure 2B):

$$\tau = \tau_y + K\dot{\gamma}^n$$
, Equation 1

where  $\tau$  is the applied shear stress,  $\dot{\gamma}$  is the shear rate,  $\tau_y$  is the shear yield stress, n is the shear thinning coefficient, and K is the viscosity parameter. <sup>35</sup> At all temperatures, the matrix exhibits shear thinning behavior, with n < 1 and K increasing with temperature (Table S1). The flow ramps also show hysteresis. The static yield stress,  $\tau_y^{Stat}$ , measured when raising the shear rate, is higher than the dynamic one,  $\tau_y^{Dyn}$ , recorded for a decreasing shear rate. Both  $\tau_y^{Stat}$  and  $\tau_y^{Dyn}$  increase with temperature (Figure 2C; Table S1).

To enable the omnidirectional movement of the printing nozzle within it, the matrix structure should be broken at relatively low stresses ( $\tau_y^{Stat}$ ). As the nozzle passes, the internal friction of the matrix at the wake of the nozzle converts strain energy to





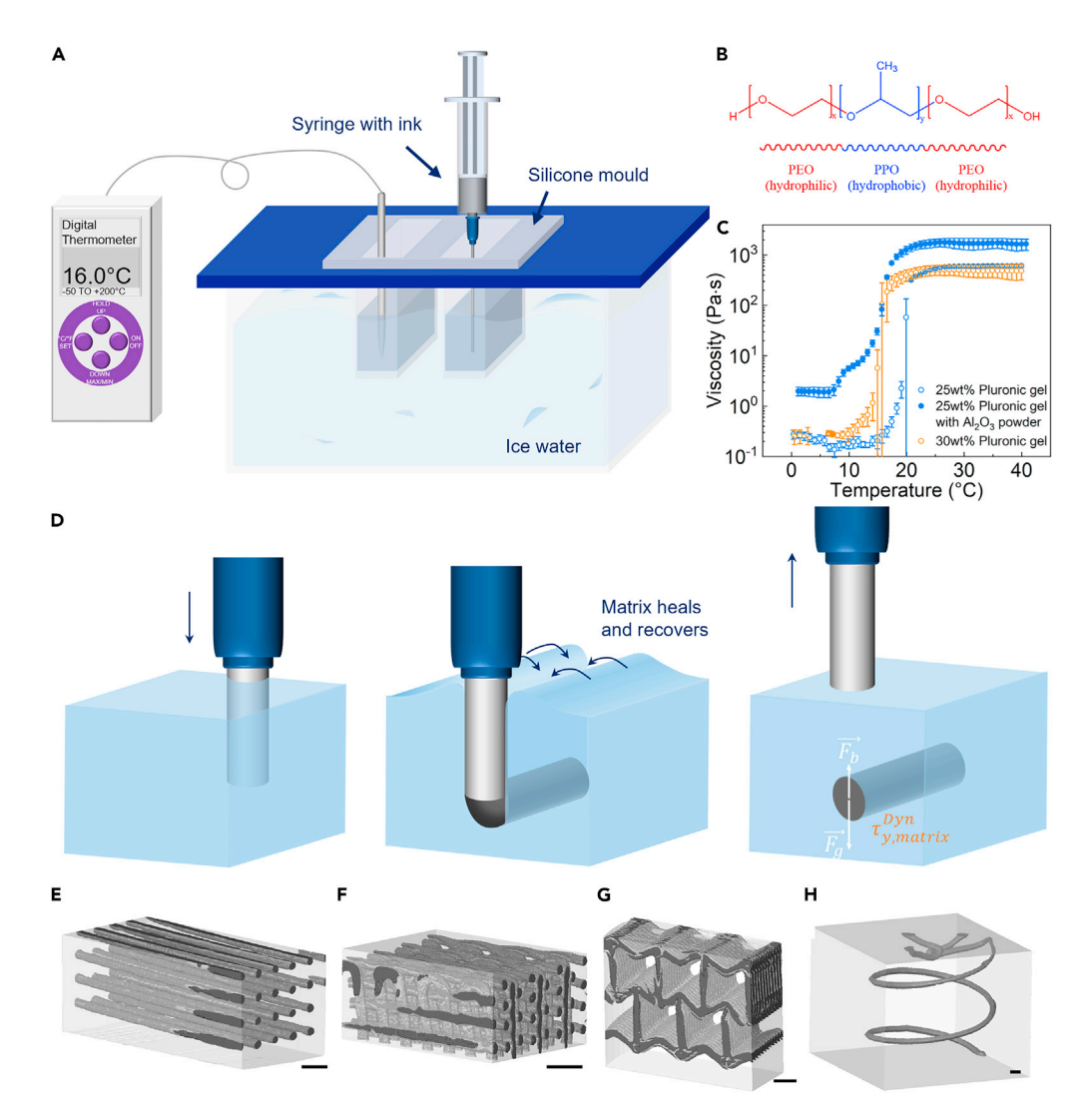


Figure 1. Embedded printing process and examples of printed composites

(A) Schematics of embedded 3D printing. The matrix suspension is gel casted in a silicone mold and the ink suspensions extruded according to a CAD model.

- (B) Chemical structure of Pluronic F127.
- (C) Viscosity-temperature curve of 25 wt % and 30 wt % Pluronic gel and the gel with inorganic powder. Error bars represent the standard deviation.
- (D) Illustration of the embedded printing process. First, the nozzle tip goes into the matrix suspension and then travels according to CAD models as the ink is being extruded. The matrix behind the nozzle flows back to heal the gap, and finally the nozzle is removed after the whole structure is printed and sustained in the position.
- (E-H) 3D X-ray CT volume rendering of the steel and microchannel structures (rendered dark gray) embedded in Al<sub>2</sub>O<sub>3</sub> matrices (rendered light gray). Scale bar, 1 mm.
- (E) Unidirectional steel fiber array.
- (F) Steel woodpile structure.
- (G) Steel auxetic structure.
- (H) Spiral channel with three inlets in  $Al_2O_3$ .

thermal energy, leading to hysteresis during reconstruction of the gel network. After the nozzle has passed, the matrix should flow to fully heal the crevice and recover enough strength  $(\tau_y^{Dyn})$  to hold the weight of the printed part.

To demonstrate the capabilities of embedded printing, inks containing two inorganic powders with very different densities (steel and graphite) were extruded in





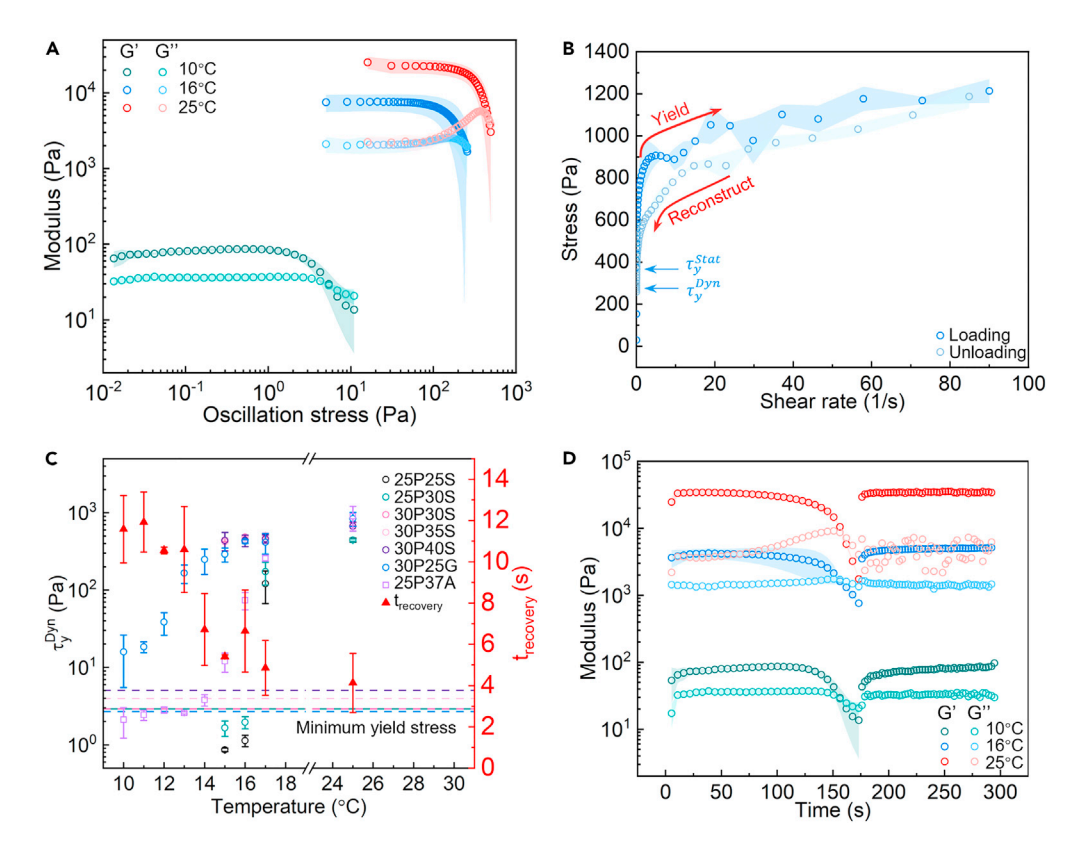


Figure 2. The rheological properties of the inks and matrices

- (A) Oscillatory test of Al<sub>2</sub>O<sub>3</sub> matrix suspension at 10°C-25°C.
- (B) Illustration of hysteresis stress measurement of  $Al_2O_3$  matrix suspension at  $17^{\circ}C$ .

(C) Recovery time of  $Al_2O_3$  matrix printable (solid symbols) and dynamic yield stress of the matrix and inks (open symbols) as a function of temperature. The minimum yield stress depending on the density of the ink (Equation 2) is labeled with dashed lines in the color corresponding with the ink composition. The notation describes the Pluronic and solid content with S for steel, G for graphite, and A for alumina. For example, 25P25S represents 25wt % Pluronic 25 vol % steel. Error bars represent the standard deviation.

(D) Two-step modulus recovery tests of the  $Al_2O_3$  matrix.

an alumina matrix. The powders were mixed with Pluronic gels to formulate pastes for extrusion. As with the matrix, the inks should have solid contents large enough as to form dense structures upon sintering and below the packing limit to facilitate extrusion (Figures 3iii and S3).

All graphite and steel inks exhibit a shear thinning behavior with shear thinning coefficients in the range of 0.1–0.5. The inks also exhibit hysteresis in the flow measurements with  $\tau_y^{Stat} > \tau_y^{Dyn}$  (Table S1). After the filaments are extruded in the Al<sub>2</sub>O<sub>3</sub> matrix, they can move downward or upward, depending on the balance between gravity  $\overrightarrow{F_g} = \rho_{ink} \overrightarrow{g} \pi r^2 L$  and buoyancy  $\overrightarrow{F_b} = -\rho_{matrix} \overrightarrow{g} \pi r^2 L$ , where  $\rho_{matrix}$  is the density of matrix suspension,  $\rho_{ink}$  is the density of ink suspension,  $\overrightarrow{g}$  is the acceleration of gravity, r is the radius of the ink filament, and L is its length. The maximum stress that the matrix can apply on the circumference of ink filaments against their displacement or distortion and prevent the horizontal filaments from sinking or floating is equal to the yield stress of the matrix. The minimum yield stress required to avoid filament displacement could be estimated as:

$$\rho_{\textit{matrix}} g \pi r^2 \mathsf{L} \pm 2 r \tau_{\textit{y,matrix}}^{\textit{dyn}} \mathsf{L} \geq \rho_{\textit{ink}} g \pi r^2 \mathsf{L} \ \tau_{\textit{y,matrix}}^{\textit{dyn}} \geq \left| \frac{\pi g r (\rho_{\textit{ink}} - \rho_{\textit{matrix}})}{2} \right|, \qquad \text{Equation 2}$$



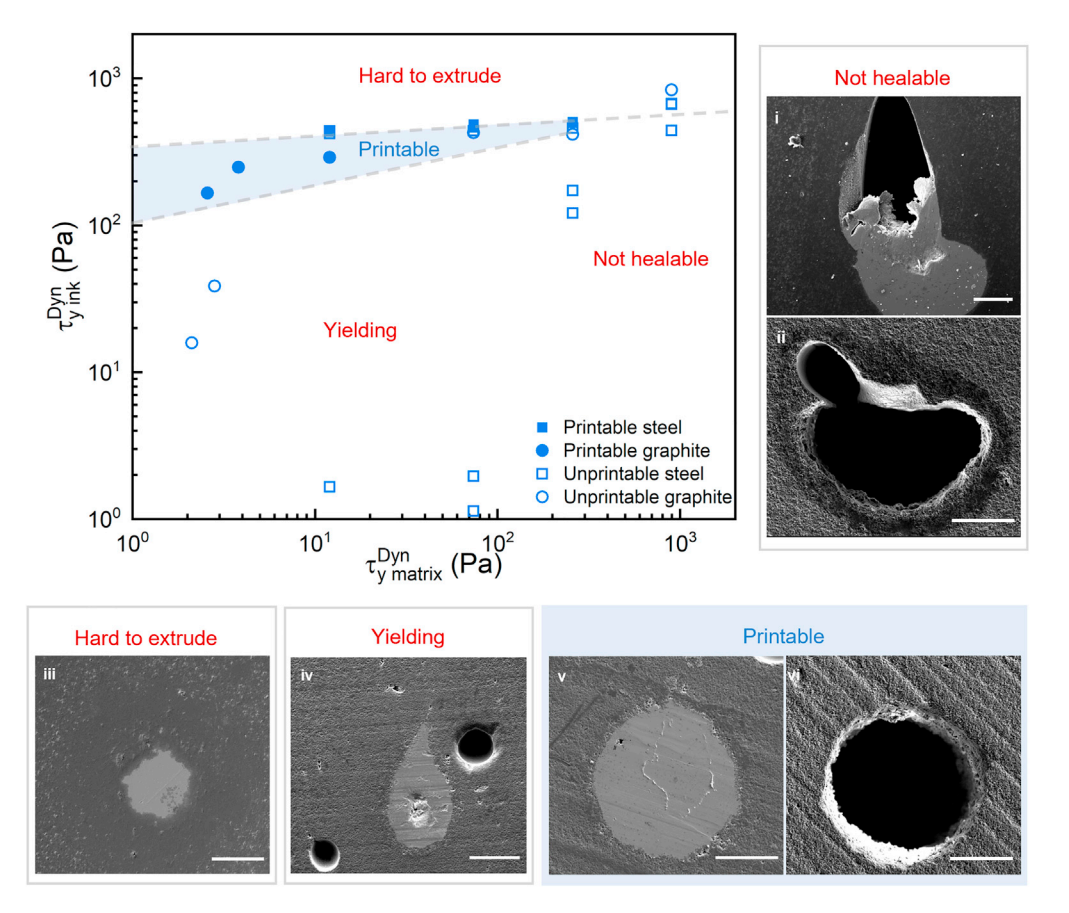


Figure 3. Printability window of embedded printing composites

Dynamic yield stress of printable (solid symbols) and not printable (open symbols) combinations of ink and matrix suspensions.

SEM images of not printable combination of ink and matrix suspensions: (i) 30P30S filaments printed in  $Al_2O_3$  matrix at  $17^{\circ}C-18^{\circ}C$ ; (iii) 30P25G filaments printed in  $Al_2O_3$  matrix at  $16^{\circ}C-17^{\circ}C$ ; (iii) 30P40S filaments printed in  $Al_2O_3$  matrix; (iv) 25P25S filaments printed in  $Al_2O_3$  matrix at  $16^{\circ}C-17^{\circ}C$ ; (vi) 30P25G filaments printed in  $Al_2O_3$  matrix below  $15^{\circ}C$ . Scale bar,  $100 \, \mu m$ .

where  $au_{y,matrix}^{dyn}$  is the dynamic yield stress of the matrix. This minimum yield stress varies with the composition and its value for steel and graphite inks in Al<sub>2</sub>O<sub>3</sub> matrices are summarized in Table S1. Filaments printed in a matrix with  $au_{y,matrix}^{Dyn}$  below this minimum will float or sink. Below 15°C, the yield stress of the matrix is below 10 Pa, which means it cannot provide effective support for structures printed with a dense ink. Above 15°C,  $au_{y,matrix}^{Dyn}$  > 70 Pa, and the matrix can hold the printed structure in place without distortion.

Healing of the gaps left by the nozzle depends on the balance between the hydrostatic pressure at the printing depth that will drive the flow to close them and the dynamic yield stress of the matrix that will resist that pressure. The gaps remain when  $\tau_y^{Dyn}$  is higher than the hydrostatic pressure; therefore, the minimum printing depth, h, to fully heal the gaps can be estimated as  $h = \frac{\tau_y^{Dyn}}{\rho_{matrix} g}$ . Considering the properties of our matrix, gaps can be completely healed with a printing depth larger than 3.6 mm below 17°C and more than 12.5 mm above 17°C.

The time that it takes the matrix to recover its properties after being broken by the passing nozzle is also critical. It determines whether the printed part will have time to move and deform before the matrix is able to hold it. It can be evaluated by the





response of storage modulus G' or viscosity as a function of time during recovery tests. <sup>12,18</sup> At 10°C, it takes more than 10 s for the matrix to fully recover (Figure 2D); this is too long, as it allows the printed filaments to sink or float before the matrix regains its strength. The recovery time decreases with rising temperature (Figure 2C) being around 5 s between 15°C and 17°C and 4 s at 25°C. For samples printed at the highest temperature, 25°C, a gap appears between the printed filament and the matrix (Figures 3i and 3ii). The recovery of matrix to its gel-like properties is too fast to enable enough flow to heal the crevice left by the nozzle. As a result, printing temperatures around the liquid-gel transition temperature (10°C–17°C) are used to achieve a defect-free matrix, while faithfully retaining the features of the printed structure.

In direct ink writing, the yield stress of the ink determines the ability to retain the shape of the printed parts. Steel inks with a Pluronic content of 25 wt % lose their shape at the printing temperature because their  $\tau_{y}^{Dyn}$  is too low (Figures 2C and 3iv). By increasing the Pluronic fraction from 25 wt % to 30 wt %, the  $\tau_{\nu}^{Dyn}$  of the ink becomes sufficient to print filaments that retain a circular cross-section (Figure 3v). For graphite inks,  $\tau_{v}^{Dyn}$  always exceeds the minimum yield stress required when the printing temperature is above 15°C, resulting in round microchannels in the Al<sub>2</sub>O<sub>3</sub> matrix (Figures 1H and 3vi). Filament rupture can also arise during embedded printing. It happens when the continuous filaments bead up and form droplets due to the Plateau-Rayleigh instability. However, this does not take place for the filament diameters used in this work (see supplemental information). Recent simulations and experiments also show that when printing Herschel-Bulkley inks in Herschel-Bulkley matrices, the ratio between the viscosities of the ink and the matrix will also play a role on the filament shape. The filament will flatten when the viscosities of fluid and matrix are high. 28,36 We have observed filament flattening when printing graphite filaments if both the matrix and filament have larger yield stresses (usually in our system, higher yield stress means higher viscosity). Similarly, when the viscosities are low or there is poor matching between the viscosity of the matrix and the ink, the filament will have a droplet cross-section like the one observed here for the steel inks (Figure S4). In general, both simulations and experiments suggest that a high viscosity ratio between ink and matrix is needed to retain a round filament cross-section. However, in our case the viscosities of ink and matrix during printing are always similar in all cases. There are some differences between these works and our experiments; in our systems, there is a much greater difference between the densities of matrix and inks and the yield stresses are also bigger.

#### Case study 1: Printing dense steel fibers

We have taken advantage of embedded 3D printing to introduce steel reinforcing structures into  $Al_2O_3$ . After printing, the samples are dried and sintered. Drying is a critical step in the fabrication of the parts so as to avoid cracking. We have performed *in situ* X-ray tomography to visualize the possible generation of cracks during the drying step (Figure S5). The results demonstrate that it is necessary to control humidity in the atmosphere carefully. As a result, we have chosen natural drying (close to room temperature) at  $72\% \pm 3\%$  humidity. This is often used in the ceramic industry and the drying times of a few weeks for samples tens of millimeters in size are comparable with current practice.  $^{34,37-39}$  If necessary, drying times can be shortened considerably by increasing the temperature or adjusting the humidity.  $^{37,38}$  While gel casting will have limits on the largest size that can be produced, in practice parts as thick as 5 cm have been made by this method.  $^{37}$  After sintering, our samples are dense (porosity below 10%) as the melting point of the steel (1,532°C) enables it to be co-sintered with alumina in solid state. The hardness of steel and alumina in



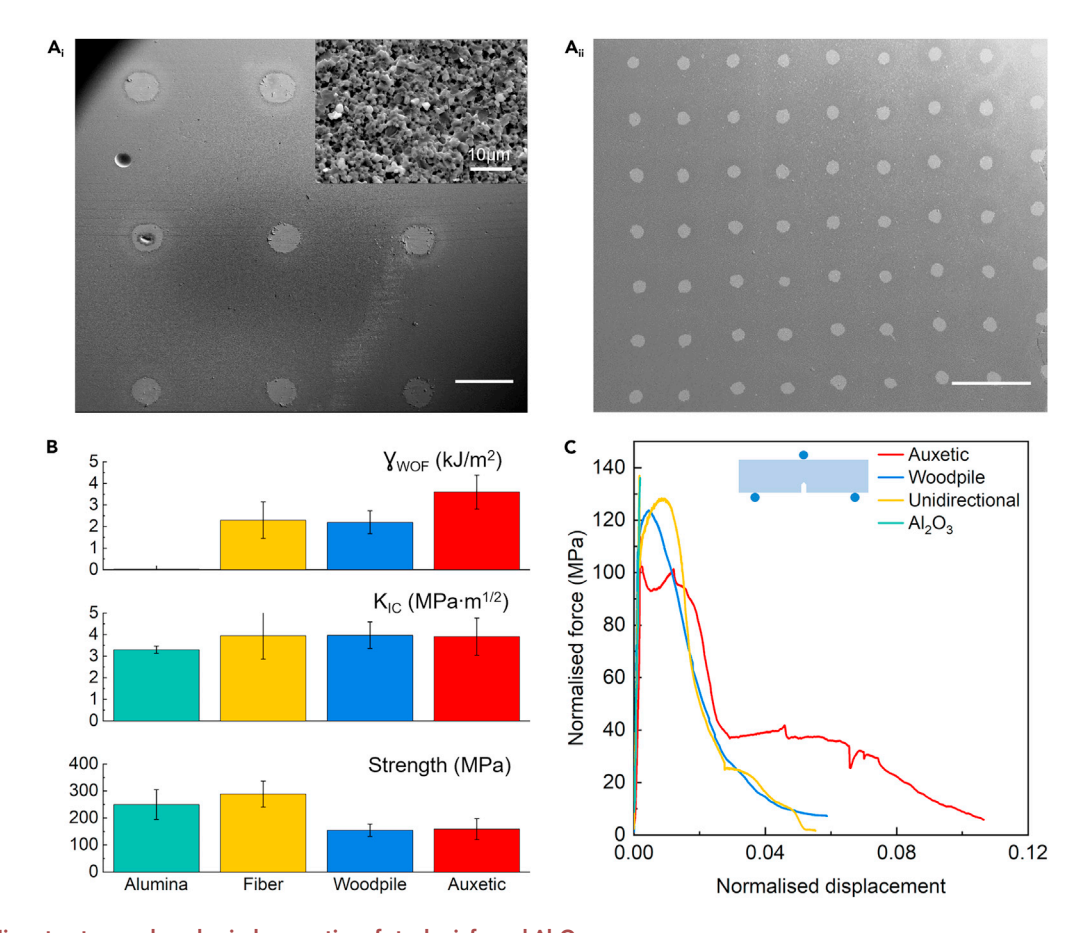


Figure 4. Microstructure and mechanical properties of steel-reinforced  $\mathrm{Al_2O_3}$ 

(A) Steel unidirectional arrays in  $Al_2O_3$  printed with a (i) 410- $\mu$ m nozzle (filament diameter  $\sim$ 260  $\mu$ m after sintering), high magnification of alumina inset and (ii) 150- $\mu$ m nozzle (filament diameter  $\sim$ 70  $\mu$ m after sintering) . Scale bar, 500  $\mu$ m.

(B) Strength, toughness, and work of fracture of  $Al_2O_3$  and its composites, 10 samples with each embedded structure for the measurement of strength and over four samples for toughness and work of fracture.

(C) Normalized force-displacement curve of Al<sub>2</sub>O<sub>3</sub> and its composites under 3-point bending.

the sintered samples, measured by nanoindentation, are consistent with the reported values for the dense materials (Figure S6).

The filament diameter can range between  $\sim\!260~\mu m$  and  $\sim\!70~\mu m$  depending on the nozzle selection (Figure 4A) with a porosity of the composites of 4%-6%. Some pores formed during gel casting and were eliminated using cold isostatic pressing before sintering. X-ray computed tomography (CT) analysis of the sintered composites printed with a 410- $\mu$ m nozzle shows that the embedded structures (unidirectional fiber arrays, woodpile, and auxetic structures) retain the original design (Figures 1E-1G). Quantitative image analysis on the X-ray CT virtual slices shows that the volume fraction of steel is the highest in the woodpile structure (~28 vol %), followed by the auxetic structure ( $\sim$ 25 vol %) and then by the unidirectional fiber array (~11 vol %). These samples were used for mechanical testing. The embedded steel fiber has a distance of 0.7 mm among unidirectional fiber arrays and 0.65 mm for woodpile structures. Despite the filaments being squeezed in woodpile structures, the radius of the filaments is the same as that in unidirectional arrays, ~0.13 mm. The unit cell of the auxetic structures is 2.3 mm in length and 2.6 mm in width. In addition, the yield stresses of the matrix and ink are high enough to avoid mixing between steel and alumina during printing. The interface is sharp





and free of porosity as demonstrated by the scanning electron microscopy (SEM) images and associated EDX elemental analysis (Figure S6).

The equivalent bending strength of all steel-alumina composites is of the same order (Figure 4B), between 155  $\pm$  23 MPa and 289  $\pm$  48 MPa, with the unidirectional fiber array exhibiting the greatest strength, despite having the lowest steel volume fraction. A decrease in the strength has been observed when embedding the more complex structures (woodpile and auxetic). This may be due to the generation of small tensile stresses in some areas of the matrix (discussed below) and/or the introduction of defects in the matrix when the printing paths are more complicated and closer together. The measured plane strain fracture toughness, K<sub>IC</sub>, is also very similar, with values of 3.3  $\pm$  0.2 MPa m<sup>1/2</sup> for pure alumina and up to 4.0  $\pm$  0.9 MPa m<sup>1/2</sup> for steel composites under 3-point bending. This is likely because, in each case, crack propagation always starts in the ceramic. The small increase in the K<sub>IC</sub> for the composites could be due to the introduction of compressive residual thermal stresses in the matrix. These strengths and toughness are comparable to those reported for alumina ceramics fabricated by gel casting or direct ink writing. 10,40-42 We used a thermomechanical finite element model (FEM) to estimate the magnitude of the residual stresses. After cooling, the compressive residual stresses in the ceramic matrix perpendicular to the loading direction are predicted to reach values up to 600 MPa (Figures 5B-5D). However, the fracture behavior is very different from monolithic alumina and the architecture of the steel reinforcement plays a significant role. Whereas the ceramic demonstrates brittle failure, samples reinforced with unidirectional fiber arrays and woodpile structures show progressive failure with a work of fracture up to  $\sim$ 2.3 kJ/m<sup>2</sup>. This is two orders of magnitude larger than the fracture energy estimated for our unreinforced alumina, ~30 J/m<sup>2</sup> according to  $G_{IC} = \frac{K_{IC}^2}{F}$ . Upon bending, the embedded auxetic steel framework shows a relatively extended plateau in the normalized force vs. displacement curve resulting in a further ( $\sim$ 50%) improvement in the work of fracture, reaching a value of 3.6 kJ/m<sup>2</sup> (Figure 4C).

To monitor how the fracture propagates in these composites, in situ bending tests were carried out in the SEM and in the X-ray CT scanner. The unidirectional fiber array and woodpile structures show similar toughening mechanisms, primarily fiber bridging and plastic deformation of the steel (Figure 5A). In samples having the woodpile reinforcement (Figure 5C), the cracks propagate along the interface between steel fibers (oriented parallel to crack propagation) and the Al<sub>2</sub>O<sub>3</sub>, while the steel fibers perpendicular to the crack plane deform plastically locally and fracture.

The fracture behavior of the Al<sub>2</sub>O<sub>3</sub> reinforced with an auxetic structure is more complex (Figure 5D). As in the other steel-reinforced ceramics, the main contributor to the fracture energy is the plastic deformation of the steel. The auxetic structure seems to maximize this contribution as the whole steel lattice plastically deforms significantly before fracturing at the nodes (Figure 5D), while for the unidirectional fiber structure, steel plasticity is confined to the regions near the crack (Figure 5A). In part, this could be the result of the crack paths guided by the distribution of residual stresses that are tensile (50-180 MPa) in the regions close to the convex corners of the steel cells and gradually become slightly compressive, up to 50 MPa, at the center of the cell (Figure 5D, insert). High compressive stresses (100-650 MPa) also develop close to the concave corners. The auxetic structure directs the propagating crack along the interface between the steel and Al<sub>2</sub>O<sub>3</sub> toward the corners of the cells where they are arrested (Figure 5D). Once the crack is arrested, further bending triggers extensive plastic deformation in the metal. In addition, the stresses



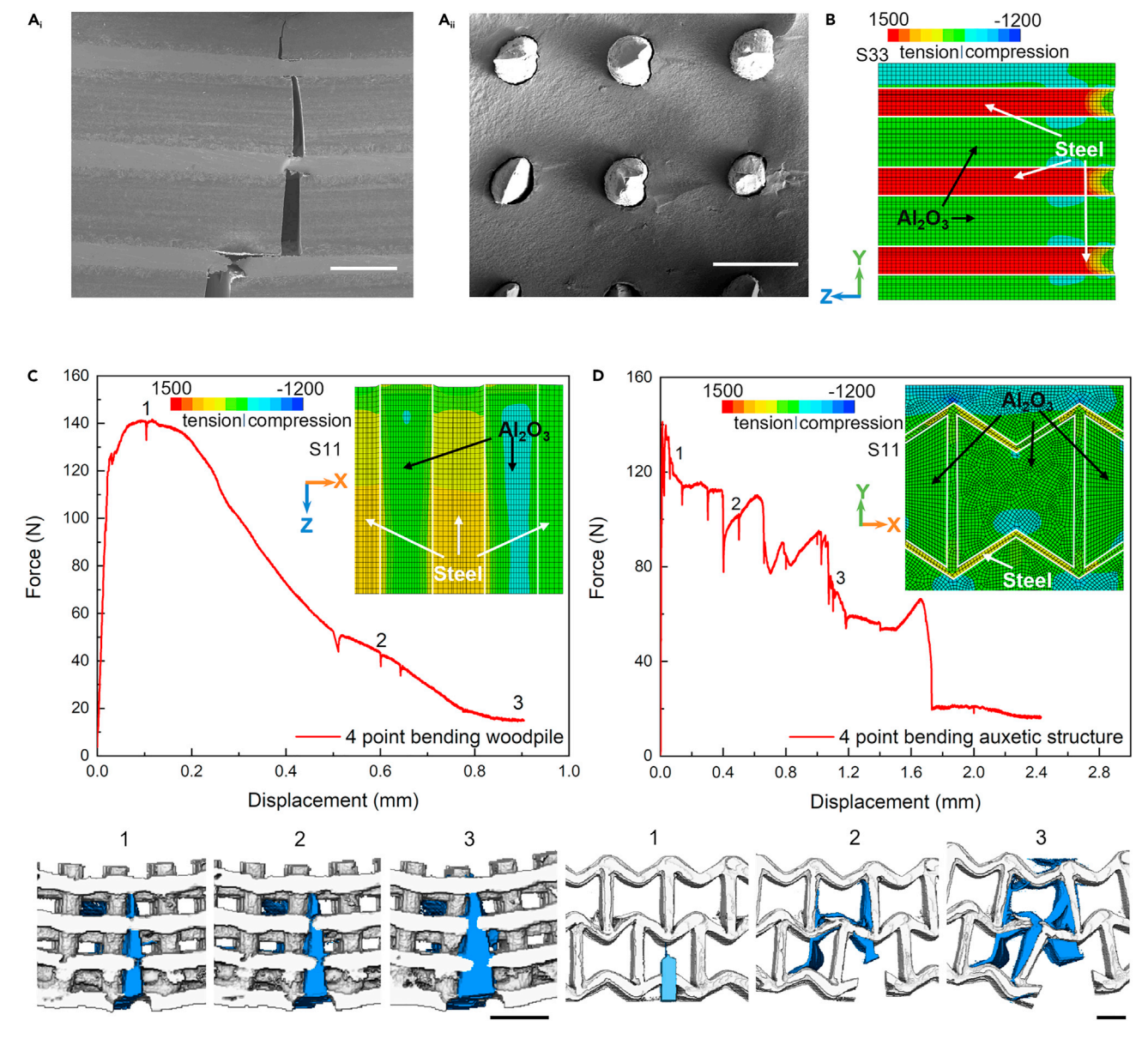


Figure 5. Fracture behavior of steel-reinforced Al<sub>2</sub>O<sub>3</sub> and finite element modeling of thermal stress

(A) (i) Longitudinal SEM image of unidirectional composite during 3-point bending and (ii) its fracture surface. Scale bar, 500 µm. (B–D) Finite element modeling of thermal stress introduced cooling from the sintering temperature for unidirectional (B), woodpile (C, insert), and auxetic structures reinforced  $Al_2O_3$  composites (D, insert). The unit of stress is MPa. The force displacement curve of woodpile (C) and auxetic structures reinforced Al<sub>2</sub>O<sub>3</sub> composites (D) during in situ four-point bending and the corresponding volume renderings of X-ray CT revealing the development of crack, the ceramic rendered transparent, the crack dark blue, the notch light blue and the steel framework light gray. Scale bar, 1 mm.

in the auxetic structure promote crack branching and multiple arrest points that contribute to increased plastic deformation and the overall work of fracture.

One of the problems that arises when designing ceramic composites is the need to balance strength and toughness. Usually, an increase in one means a substantial decrease in the other. 43 Our results show that, by using embedded printing of metallic fibers in a ceramic matrix, it is possible to increase the work of fracture while largely retaining strength. Furthermore, the technique enables the introduction of reinforcement architectures designed to engineer residual stresses, direct crack





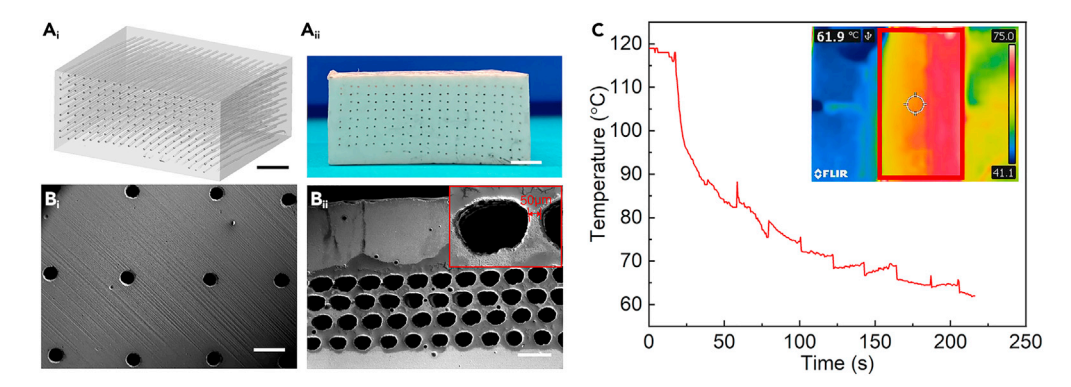


Figure 6. Embedded printing of sacrificial filaments for thermal management

(A) (i) 3D X-ray CT volume rendering and (ii) and a cross-section of a large  $Al_2O_3$  cube with straight microchannels printed with an 0.41-mm stainless steel tip. Scale bar, 5 mm.

(B) Close up of 200- $\mu$ m-diameter microchannels in Al<sub>2</sub>O<sub>3</sub> printed with (i) 2 mm and (ii) 0.5 mm spacings. Scale bar, 500  $\mu$ m.

(C) The change in temperature on the surface of  $Al_2O_3$  microchannel cube upon flushing cold water through the channels (fluctuations are due to the infrared camera being recalibrated every 25 s). (Insert) The thermal images of  $Al_2O_3$  (labeled with the red box) and clamps viewed from the top after cooling.

propagation, and maximize toughening, in this case by promoting the contribution of plasticity. These results show that the integration of metamaterial structures could open new opportunities in composite design. Although there has been very significant progress in the development of metamaterials with unique properties, they often have open cell structures that can limit their practical implementation. 44–46 Embedded printing opens the possibility to integrate these metamaterials in dense composites that could exhibit unprecedented performance.

#### Case study 2: Printing sacrificial graphite filaments

Embedded 3D printing can also be used to introduce microchannels having a variety of complex 3D geometries into ceramic bodies in one simple step, without the need for laser cutting <sup>47</sup> or washing a prefabricated template. <sup>48</sup> Here, we print sacrificial graphite filaments in an Al<sub>2</sub>O<sub>3</sub> matrix and the microchannels are then formed by the burn-out of carbon during sintering. We use the method to create straight microchannel arrays (Figure 6A) and spiral microchannels (Figure 1H). The cross-section of the channels is circular with a diameter around 200 µm after sintering when printing at 15°C (Figure 3vi), whereas droplet-shaped cross-sections (Figure 3ii) form above 15°C due to mismatch between the viscoelastic properties of the matrix and the ink. The effect of the distance between filaments was investigated by printing filaments with separations of 2 mm and 0.5 mm with a 410-μm stainless steel cylindrical tip at 14°C–15°C (Figure 6B). The thickness of the wall between filaments can be reduced down to  $\sim$ 50  $\mu$ m (Figure 6Bii). The ceramic matrix pre-sinters at the carbon burn-out temperature so that it does not collapse to close the microchannels (Figure S7). However, if the filaments become closer, they deform. This arises from the velocity field generated in the Herschel-Bulkley fluid around the moving cylindrical tip. 12 With a closer inter-filament distance, this velocity field affects the previously printed filaments and leads to deformation.

Channel connectivity is evident from the X-ray CT result (Figure 6A). The potential of such an arrangement is demonstrated by flowing cold water (0°C–4°C) at a rate of 5.1 mL/min through a 21 × 10 channel array with the diameter of each channel ~200  $\mu$ m (Figure 6B) in an alumina cube (2.6 × 2.6 × 1.5 cm³) heated on a hot plate at 300°C (Figure S8). Figure 6C shows the temperature change at the top surface of the Al<sub>2</sub>O<sub>3</sub> cube. The temperature in the center falls from 119°C to 62°C in 200 s, consistent with good, continuous water flow (Video S2).





#### **Conclusions**

We have developed embedded 3D printing as a means of printing complex structures within dense ceramics. This is achieved by extruding ceramic inks inside a self-healing ceramic gel. To ensure high printing fidelity and the formation of a dense, defect-free material, a number of conditions must be met:

- (1) The viscoelastic response of the ink and the matrix gel must be matched to enable the matrix to support the embedded phase without significant move-
- (2) The matrix gel should break at low stresses to enable the movement of the nozzle in its interior and the extrusion of the ink.
- (3) The matrix gel must flow to ensure healing but recover its properties (stiffness and strength) fast enough to support the printed structure.
- (4) The ink should be extrudable but with a high dynamic yield stress to avoid deformation.
- (5) Both matrix and inks should also have a high inorganic content to generate a dense, defect-free material after sintering.

To achieve these goals, we developed matrix and ink gels based on thermally reversible Pluronic hydrogels and manipulated their viscoelastic response by controlling the printing temperature, solid loading, and Pluronic concentration. In particular, it was observed that, for successful printing, the temperature should be close to the liquid-gel transition of the matrix.

As models to showcase the printing of complex shapes in a dense ceramic and to illustrate the benefits of the technique, we have used embedded printing to introduce steel and graphite structures within an alumina matrix. The diameter of the printed filaments ranges between 70 and 260 microns after sintering. The technique enables the introduction of embedded auxetic steel structures that generate fracture energies orders of magnitude above that of the ceramic and are significantly higher than those reached with grids or parallel fiber arrangements. The graphite acts a sacrificial vehicle to create complex, 3D microchannel arrays inside the ceramic. These results suggest that embedded printing is a viable alternative for the fabrication of multi-material inorganic structures. It may be possible to find additional formulations to support embedded printing in inorganic matrices and to open new opportunities for the design of composites incorporating metamaterial reinforcements and devices for structural and functional applications.

### **EXPERIMENTAL PROCEDURES**

#### Resource availability

#### Lead contact

Further information and requests for resources and reagents should be directed to and will be fulfilled by the lead contact, Shitong Zhou (s.zhou18@imperial.ac.uk).

#### Materials availability

This study did not generate new unique reagents.

#### Data and code availability

All data supporting the findings of this study are available within the paper and its supplemental information or from the corresponding authors upon reasonable request. This study did not generate a code.





#### Preparation of ink and matrix suspensions

Pluronic F127 powder (Sigma-Aldrich) was dissolved in distilled water and stored in a fridge at 0°C–4°C for 24 h to obtain 25 wt % and 30 wt % Pluronic gels. Alumina (SMA6, Baikowski) with a  $d_{50}$  of 0.2  $\mu m$  was sieved using a 100  $\mu m$  plastic sieve to reduce the likelihood of agglomeration. The matrix slurry was prepared by adding the alumina powder to a 25 wt % Pluronic gel in a weight ratio of 7:3. Dolapix CA was added as a dispersant, 1 wt % with respect to the  $Al_2O_3$  powder. This mixture was homogenized in a Thinky ARE-250 planetary mixer at 2,000 rpm for 2 min, after chilling in an ice bath. The mixing and chilling steps were repeated three to five times until a homogeneous  $Al_2O_3$  suspension was obtained with no remaining powder agglomerates. After the suspension was defoamed at 2,200 rpm for 10 min to remove internal bubbles, it was cooled down below 13°C and then gel cast in a silicone mold greased with silicone oil to facilitate mold release. An additional degassing step in a vacuum desiccator was performed to get rid of air trapped during gel casting.

The steel ink was prepared by mixing different volume ratios (25–40 vol %) of steel powder (430 L, 5  $\mu m$  average particle size; US Research Nanomaterials) with a 25 wt % or a 30 wt % Pluronic gel and adding 0.5 wt % Dolapix to the mass of steel powder. The mixing and defoaming steps were the same as those mentioned above. The homogeneous steel ink was placed in a 3-mL syringe barrel using a spatula and then transferred to another printing 3-mL syringe barrel using a syringe-syringe Luer-lock connector to avoid trapping air. The graphite ink comprising a 30 wt % Pluronic gel and graphite powder (7–11  $\mu m$  particle size, 99%, Alfa Aesar) in a volume ratio of 3:1, was mixed and transferred to the syringe barrels in the same way as the steel ink.

#### Embedded printing in a ceramic matrix

Printing patterns and parameters were defined using G-code for spiral structures and the remaining patterns with RoboCAD software (3dlnks). Steel and graphite filaments were printed using a robocaster system (3dlnks) with a printing speed of 6 mm/s and stainless steel tip nozzles with an inner diameter of 0.15 mm (outer diameter of 0.31 mm) and 0.41 mm (outer diameter of 0.72 mm). The printing distance between steel and graphite filaments on the cross-section was varied from 0.5 mm to 3 mm. For mechanical tests, the bars with unidirectional steel fiber arrays, auxetic, and woodpile structures were printed in Al $_2$ O $_3$  matrices at 3 mm/s. The temperature of the Al $_2$ O $_3$  matrix suspension was adjusted between 10°C and 18°C by placing the silicone mold in an ice bath and measured while printing using a thermometer. A humidifier in the enclosure system was used to keep the humidity at 75%  $\pm$  10% and inhibit water evaporation from the surface, which could cause crack formation of the final products.

#### **Drying and sintering**

Drying was performed both in air and a high-humidity convection oven. The humidity in the oven, measured with a Thorlabs TSP01 sensor, was controlled at  $72\% \pm 3\%$  by placing a supersaturated NaCl solution inside. The temperature of this oven was set at  $32^{\circ}$ C, and a fan was placed in it to promote air circulation. Drying typically lasted for 2 weeks for  $16 \times 16 \times 16$  mm cubes and  $33 \times 10 \times 12$  mm bars and took longer for bigger samples. This drying time can be significantly decreased with well controlled humidity and temperature.  $^{37,38}$  Dried samples were densified by cold isostatic pressing (Stansted Fluid Power LTD) at 300 MPa for 5 min to close the pores formed during casting of the matrix and avoid defects. To ensure that the Pluronic was gradually and completely burnt out without the generation of cracks, de-binding was first conducted in a chamber lift furnace with a heating rate of  $1^{\circ}$ C/min from room temperature to  $350^{\circ}$ C and held for 1 h. After reaching  $500^{\circ}$ C





with a heating rate of  $2^{\circ}$ C/min, the temperature was maintained for 2 h before cooling down. The steel reinforced Al<sub>2</sub>O<sub>3</sub> composites were densified in a vacuum furnace by increasing the temperature to  $600^{\circ}$ C at a heating rate of  $10^{\circ}$ C/min, before holding for 1 h. After that, the temperature was increased to  $1,450^{\circ}$ C using the same rate and maintained for 2 h before cooling down to room temperature. To sinter the matrix and burn out the graphite in the Al<sub>2</sub>O<sub>3</sub>/graphite to create microchannels, after de-binding at  $500^{\circ}$ C the samples were further sintered in a chamber lift furnace to  $1,550^{\circ}$ C at a heating rate of  $5^{\circ}$ C/min.

#### **Rheological measurements**

The rheological behavior of matrix and ink suspensions was analyzed using a TA Instruments Discovery HR-1 rheometer with a 40-mm parallel plate geometry and a 1,000- $\mu$ m gap. A few droplets of distilled water were placed on the solvent gap to prevent evaporation. The shear rate increased from 0.01  $s^{-1}$  to 100  $s^{-1}$  in 60 s during flow ramps and oscillatory tests were carried out from 1 to 2,000 Pa at a fixed frequency of 1 Hz in amplitude sweeps. Hysteresis stress measurements were used to determine the yield stress to initiate ink flow and during the recovery. In the measurement, the shear rate went up from 0.01  $s^{-1}$  to 100  $s^{-1}$  and down to 0.01  $s^{-1}$ . To simulate the Al<sub>2</sub>O<sub>3</sub> matrix during printing and to monitor the matrix response as a function of time, a two-step modulus recovery test was performed by first increasing stress from 1 Pa to 1,000 Pa and then keeping a low stress of 0.5 or 5 Pa. The recovery time was considered as the earliest point where storage modulus G' did not obviously increase with time, and the degree of recovery was calculated by dividing the storage modulus at the end by the initial storage modulus. Temperature ramp measurements were performed from 0°C to 40°C at a fixed shear rate of 1  $s^{-1}$ .

#### Characterization

The microstructure of the as received powder and the polished sintered samples was observed using a JOEL 6010 SEM at 20 kV after a thin gold film was coated on the surface to improve conductivity. X-ray micro-CT was used to investigate evolution of the internal structure of the Al<sub>2</sub>O<sub>3</sub> gel matrix during dying. A Zeiss Versa 520 X-ray microscope was used to continuously scan the gel as it dried in air. The X-ray tube operated at an accelerating voltage of 80 kV and a power of 7 W. A doped glass (LE5 filter from Zeiss) energy filter was applied after the source to remove the low-energy photons and improve the transmission rate. Each tomographic scan comprised 1,601 projections taken incrementally as the sample was rotated by 360°. For each projection, an exposure time of 2.5 s was used and each tomographic scan took  $\sim$ 1.1 h to complete. The reconstructed volumes had a voxel size of 11.2  $\mu$ m covering a field of view of  $\sim$ 22  $\times$  22  $\times$  22 mm<sup>3</sup>. The as-printed Al<sub>2</sub>O<sub>3</sub> with microchannels was scanned using a Nikon Xtek High Flux Bay operating at 120 kV and a power of 10 W with 3,179 projections recorded using a flat panel detector. The reconstructed volume had a voxel size of 5.4  $\mu$ m. For the steel composite samples, the same setup was used but with the X-ray tube operated at 210 kV. This was combined with a 0.25-mm Cu energy filter to harden the X-ray beam. We recorded 2,000 projections for each scan and the reconstructed volume had a voxel size of 11 μm. Image analysis was conducted using Avizo 9.3 software. The voxels representing the channels and steel reinforcements were picked out using regiongrowing and gray value thresholding. Dimensions of these features were determined from the segmented images. For microchannels, Al<sub>2</sub>O<sub>3</sub> cubes as large as  $2.6 \times 2.6 \times 1.5 \text{ cm}^3$  with multiple straight microchannels and  $1.4 \times 1.4 \times 1.1 \text{ cm}^3$ with a spiral microchannel were printed with steel cylindrical tips.





Mechanical testing includes three-point bending to measure bending strength on ten polished samples for each structure with the tensile surfaces polished down to 1  $\mu$ m and toughness using over four polished single-edge notched bend (SENB) samples (25 × 3 × 3 mm³ for composites with unidirectional arrays and woodpile structures and 25 × 6 × 3 mm³ for composites with auxetic structures) according to ASTM E1820. The strength  $\sigma_f$ , fracture toughness  $K_{IC}$  and work of fracture  $\gamma_{WOF}$  were calculated by:<sup>49</sup>

$$\sigma_{f} = \frac{3FL}{2BW^{2}}$$

$$K_{IC} = \frac{3FL}{2BW^{2}} \times \left(\frac{a}{W}\right)^{\frac{1}{2}} \times \frac{1.99 - \frac{a}{W} \times \left(1 - \frac{a}{W}\right) \left(2.15 - 3.93 \frac{a}{W} + 2.7 \left(\frac{a}{W}\right)^{2}\right)}{\left(1 + 2\frac{a}{W}\right) \left(1 - \frac{a}{W}\right)^{\frac{3}{2}}}$$

$$\gamma_{WOF} = \frac{W_{f}}{2A_{CS}},$$

where F is the applied force where the force-displacement curve stops being linear, L is the support span, B is the width, W is the thickness, a is the crack length, A<sub>CS</sub> is the area of fracture surface,  $W_f$  is the total energy of the fracture process given by  $\int Fd\delta$ , and  $d\delta$  is the change of displacement of sample. The SENB specimens were notched with a 0.25 mm diamond wafering blade, the notch was sharpened with a razor blade and 1-μm diamond suspension. The tests were carried out on a Zwick iLine universal testing machine with a span of 15 mm at a displacement rate of 0.1 mm/min with the displacement corrected using a high-resolution camera. Crack propagation during bending was observed in situ using three-point bending tests in the SEM and four-point bending tests in X-ray CT. The tests within the SEM were performed using an MT300 Tensile Tester (DEBEN) with a span of 21 mm. Tests within X-ray CT were performed using a Deben CT5000 tensile/compression stage with an inner span of 6 mm and an outer span of 20 mm. All in situ tests used the same 0.1-mm/min displacement rate. The sample together with the rig was scanned using the Nikon Xtek High Flux Bay with the same settings used for the as-printed composites. The connectivity and cooling performance of the microchannels in Al<sub>2</sub>O<sub>3</sub> were tested by flushing iced water through them. The iced water flux was controlled with a peristaltic pump (Watson Marlow SCI 400) at 5.1 mL/min and the temperature of the iced water and outlet tube was recorded. Temperature in the center of the Al<sub>2</sub>O<sub>3</sub> was monitored from a top view with forward looking infrared camera (FLIR C2).

#### Finite element modeling of thermal stress during sintering

FEM of thermal stresses in steel/alumina composites was conducted on the ABAQUS platform. The dimensions of sintered samples mentioned above were used and a symmetric boundary condition was applied to reduce the size of the modeling parts and allocate more meshes (150,000–240,000 C3D8R hexahedral elements). Plastic deformation of steel was considered for the calculation and parameters including Poisson's ratio, elastic modulus, and plastic modulus were temperature dependent, <sup>50,51</sup> as listed in Table S2.

#### **SUPPLEMENTAL INFORMATION**

Supplemental information can be found online at https://doi.org/10.1016/j.matt. 2023.10.031.

# **Matter** Article



#### **ACKNOWLEDGMENTS**

This research was supported under MAPP: EPSRC Future Manufacturing Hub in Manufacture using Advanced Powder Processes (EP/P006566/1). S.Z. acknowledges financial assistance from the China Scholarship Council (No. 201806120001). This work was supported by the Henry Moseley X-ray Imaging Facility (funded through EPSRC grants EP/F007906/1, EP/F001452/1, EP/I02249X, EP/M010619/1, EP/ F028431/1, EP/M022498/1, and EP/T02593X/1) within the Henry Royce Institute for Advanced Materials (funded through EPSRC grants EP/R00661X/1, EP/ S019367/1, EP/P025021/1, and EP/P025498/1).

#### **AUTHOR CONTRIBUTIONS**

Conceptualization, S.Z. and E.S.; methodology, S.Z., F.B., and E.S.; investigation, S.Z., Y.H., H.P., and X.Z.; writing - original draft, S.Z.; writing - review and editing, S.Z., I.T., X.Z., P.W., F.B., and E.S.; funding acquisition, P.W. and E.S.; supervision, I.T., F.B., and E.S. All authors discussed the results and commented on the manuscript.

#### **DECLARATION OF INTERESTS**

The authors declare no competing interests.

Received: July 26, 2023 Revised: October 4, 2023 Accepted: October 30, 2023 Published: November 22, 2023

#### **REFERENCES**

- 1. Hu, P., Dong, S., Zhang, X., Gui, K., Chen, G., and Hu, Z. (2017). Synthesis and characterization of ultralong SiC nanowires with unique optical properties, excellent thermal stability and flexible nanomechanical properties. Sci. Rep. 7, 3011. https://doi.org/ 10.1038/s41598-017-03588-x.
- 2. Cheng, Y., Hu, P., Zhang, W., Ma, C., Feng, J., Fan, Q., Zhang, X., and Du, S. (2019). One-step introduction of ZrC-SiC inside carbon fabric to fabricate high homogeneous and damagetolerant composite inspired by vibration.
  J. Eur. Ceram. Soc. 39, 2251–2256. https://doi. org/10.1016/j.jeurceramsoc.2019.02.030.
- 3. Du, B., He, C., Qian, J., Wang, X., Cai, M., and Shui, A. (2019). Ablation behaviors and mechanism of ultra-thick anti-oxidation layer coating on carbon-bonded carbon fiber composites. J. Am. Ceram. Soc. 102, 7543-7552. https://doi.org/10.1111/jace.16617.
- Cheng, Y., An, Y., Liu, Y., Wei, Q., Han, W., Zhang, X., Zhou, P., Wei, C., and Hu, N. (2020). ZrB2-Based "Brick-and-Mortar" Composites Achieving the Synergy of Superior Damage Tolerance and Ablation Resistance, ACS Appl. Mater. Interfaces 12, 33246-33255. https://doi org/10.1021/acsami.0c08206
- 5. Muth, J.T., Vogt, D.M., Truby, R.L., Mengüç, Y., Kolesky, D.B., Wood, R.J., and Lewis, J.A. (2014). Embedded 3D printing of strain sensors within highly stretchable elastomers. Adv. Mater. 26, 6307-6312. https://doi.org/10.1002/ adma.201400334.

- 6. Thakkar, H., Eastman, S., Al-Naddaf, Q., Rownaghi, A.A., and Rezaei, F. (2017). 3D-Printed Metal-Organic Framework Monoliths for Gas Adsorption Processes. ACS Appl. Mater. Interfaces 9, 35908-35916. https://doi. org/10.1021/acsami.7b11626.
- 7. Feilden, E., Ferraro, C., Zhang, Q., García-Tuñón, E., D'Elia, E., Giuliani, F., Vandeperre, L., and Saiz, E. (2017). 3D Printing Bioinspired Ceramic Composites. Sci. Rep. 7, 13759. https://doi.org/10.1038/s41598-017-14236-9.
- 8. Rödel, J., Kounga, A.B., Weissenberger-Eibl, M., Koch, D., Bierwisch, A., Rossner, W., Hoffmann, M.J., Danzer, R., and Schneider, G. (2009). Development of a roadmap for advanced ceramics: 2010–2025. J. Eur. Ceram. Soc. 29, 1549-1560. https://doi.org/10.1016/j. jeurceramsoc.2008.10.015.
- 9. Peng, E., Zhang, D., and Ding, J. (2018). Ceramic Robocasting: Recent Achievements, Potential, and Future Developments. Adv. Mater. 30, e1802404. https://doi.org/10.1002/ adma.201802404.
- 10. Feilden, E., Blanca, E.G.-T., Giuliani, F., Saiz, E., and Vandeperre, L. (2016). Robocasting of structural ceramic parts with hydrogel inks. J. Eur. Ceram. Soc. 36, 2525-2533. https://doi org/10.1016/j.jeurceramsoc.2016.03.001.
- 11. Smay, J.E., Nadkarni, S.S., and Xu, J. (2007). Direct Writing of Dielectric Ceramics and Base Metal Electrodes. Int. J. Appl. Ceram. Technol. 4, 47-52. https://doi.org/10.1111/j.1744-7402. 2007.02118.x.

- 12. Grosskopf, A.K., Truby, R.L., Kim, H., Perazzo, A., Lewis, J.A., and Stone, H.A. (2018). Viscoplastic Matrix Materials for Embedded 3D Printing. ACS Appl. Mater. Interfaces 10, 23353-23361. https://doi.org/10.1021/acsami.
- 13. Wu, W., DeConinck, A., and Lewis, J.A. (2011). Omnidirectional printing of 3D microvascular networks. Adv. Mater. 23, H178-H183. https:// doi.org/10.1002/adma.201004625.
- 14. Jennifer, A., Lewis, D.B.K., Skylar Scott, M.A., Homan, K.A., Truby, R.L., and Amelia, S.G. (2018). Method of printing a tissue construct with embedded vasculature. patent application 146, 613.
- 15. Truby, R.L., Wehner, M., Grosskopf, A.K., Vogt, D.M., Uzel, S.G.M., Wood, R.J., and Lewis, J.A. (2018). Soft Somatosensitive Actuators via Embedded 3D Printing. Adv. Mater. 30, e1706383. https://doi.org/10.1002/adma.
- 16. Wehner, M., Truby, R.L., Fitzgerald, D.J., Mosadegh, B., Whitesides, G.M., Lewis, J.A., and Wood, R.J. (2016). An integrated design and fabrication strategy for entirely soft, autonomous robots. Nature 536, 451–455. https://doi.org/10.1038/nature19100.
- 17. Huang, K., Elsayed, H., Franchin, G., and Colombo, P. (2021). Embedded direct ink writing of freeform ceramic components. Appl. Mater. Today 23, 101005. https://doi.org/10 1016/j.apmt.2021.101005





- Mahmoudi, M., Burlison, S.R., Moreno, S., and Minary-Jolandan, M. (2021). Additive-Free and Support-Free 3D Printing of Thermosetting Polymers with Isotropic Mechanical Properties. ACS Appl. Mater. Interfaces 13, 5529–5538. https://doi.org/10.1021/acsami.0c19608.
- Mahmoudi, M., Wang, C., Moreno, S., Burlison, S.R., Alatalo, D., Hassanipour, F., Smith, S.E., Naraghi, M., and Minary-Jolandan, M. (2020). Three-Dimensional Printing of Ceramics through "Carving" a Gel and "Filling in" the Precursor Polymer. ACS Appl. Mater. Interfaces 12, 31984–31991. https://doi.org/10.1021/ acsami.0c08260.
- O'Bryan, C.S., Bhattacharjee, T., Niemi, S.R., Balachandar, S., Baldwin, N., Ellison, S.T., Taylor, C.R., Sawyer, W.G., and Angelini, T.E. (2017). Three-dimensional printing with sacrificial materials for soft matter manufacturing. MRS Bull. 42, 571–577. https:// doi.org/10.1557/mrs.2017.167.
- Hinton, T.J., Hudson, A., Pusch, K., Lee, A., and Feinberg, A.W. (2016). 3D Printing PDMS Elastomer in a Hydrophilic Support Bath via Freeform Reversible Embedding. ACS Biomater. Sci. Eng. 2, 1781–1786. https://doi. org/10.1021/acsbiomaterials.6b00170.
- Afghah, F., Altunbek, M., Dikyol, C., and Koc, B. (2020). Preparation and characterization of nanoclay-hydrogel composite support-bath for bioprinting of complex structures. Sci. Rep. 10, 5257. https://doi.org/10.1038/s41598-020-61606-x
- 23. Zeng, J., Kasahara, N., Xie, Z., Louis, F., Kang, D., Dekishima, Y., Kuwagaki, S., Sakai, N., and Matsusaki, M. (2023). Comparative analysis of the residues of granular support bath materials on printed structures in embedded extrusion printing. Biofabrication 15, 035013. https://doi.org/10.1088/1758-5090/acce09.
- Román-Manso, B., Weeks, R.D., Truby, R.L., and Lewis, J.A. (2023). Embedded 3D Printing of Architected Ceramics via Microwave-Activated Polymerization. Adv. Mater. 35, e2209270. https://doi.org/10.1002/adma. 202209270.
- Weeks, R.D., Truby, R.L., Uzel, S.G.M., and Lewis, J.A. (2023). Embedded 3D Printing of Multimaterial Polymer Lattices via Graph-Based Print Path Planning. Adv. Mater. 35, e2206958. https://doi.org/10.1002/adma. 202206958.
- Bhattacharjee, T., Zehnder, S.M., Rowe, K.G., Jain, S., Nixon, R.M., Sawyer, W.G., and Angelini, T.E. (2015). Writing in the granular gel medium. Sci. Adv. 1, e1500655. https://doi.org/ 10.1126/sciadv.1500655.
- Highley, C.B., Rodell, C.B., and Burdick, J.A. (2015). Direct 3D Printing of Shear-Thinning Hydrogels into Self-Healing Hydrogels. Adv.

- Mater. 27, 5075–5079. https://doi.org/10.1002/adma.201501234.
- Friedrich, L.M., Gunther, R.T., and Seppala, J.E. (2022). Suppression of Filament Defects in Embedded 3D Printing. ACS Appl. Mater. Interfaces 14, 32561–32578. https://doi.org/10. 1021/acsami.2c08047.
- Bohorquez, M., Koch, C., Trygstad, T., and Pandit, N. (1999). A Study of the Temperature-Dependent Micellization of Pluronic F127. J. Colloid Interface Sci. 216, 34–40. https://doi. org/10.1006/jcis.1999.6273.
- Vadnere, M., Amidon, G., Lindenbaum, S., and Haslam, J. (1984). Thermodynamic studies on the gel-sol transition of some pluronic polyols. Int. J. Pharm. 22, 207–218. https://doi.org/10. 1016/0378-5173(84)90022-X.
- Rassing, J., and Attwood, D. (1982). Ultrasonic velocity and light-scattering studies on the polyoxyethylene polyoxypropylene copolymer Pluronic F127 in aqueous solution. Int. J. Pharm. 13, 47–55.
- 32. Tari, G. (2003). Gelcasting ceramics: A review. Am. Ceram. Soc. Bull. 82, 43–46.
- Ayode Otitoju, T., Ugochukwu Okoye, P., Chen, G., Li, Y., Onyeka Okoye, M., and Li, S. (2020). Advanced ceramic components: Materials, fabrication, and applications. J. Ind. Eng. Chem. 85, 34–65. https://doi.org/10.1016/ j.jiec.2020.02.002.
- Janney, M.A. (1994). Gelcasting—A New Way to Form Large Near-Net-Shape Ceramic Parts. Mater. Technol. 9, 97–99. https://doi.org/10. 1080/10667857.1994.11785035.
- Herschel, W.H., and Bulkley, R. (1926). Konsistenzmessungen von Gummi-Benzollösungen. Kolloid Z. 39, 291–300. https://doi.org/10.1007/BF01432034.
- Friedrich, L.M., and Seppala, J.E. (2021). Simulated filament shapes in embedded 3D printing. Soft Matter 17, 8027–8046. https:// doi.org/10.1039/d1sm00731a.
- Gilissen, R., Erauw, J.P., Smolders, A., Vanswijgenhoven, E., and Luyten, J. (2000). Gelcasting, a near net shape technique. Mater. Des. 21, 251–257. https://doi.org/10.1016/ S0261-3069(99)00075-8.
- Omatete, O.O., Janney, M.A., and Nunn, S.D. (1997). Gelcasting: From laboratory development toward industrial production.
   J. Eur. Ceram. Soc. 17, 407–413. https://doi. org/10.1016/S0955-2219(96)00147-1.
- Brosnan, D.A., and Robinson, G.C. (2003). Introduction to Drying of Ceramics: With Laboratory Exercises (American Ceramic Society).

- 40. Richerson, D.W., and Lee, W.E. (2018). Modern Ceramic Engineering: Properties, Processing, and Use in Design (CRC press).
- Ndinisa, S.S., Whitefield, D.J., and Sigalas, I. (2020). Fabrication of complex shaped alumina parts by gelcasting on 3D printed moulds. Ceram. Int. 46, 3177–3182. https://doi.org/10. 1016/j.ceramint.2019.10.021.
- Cao, M., Yan, Q., Li, X., and Mi, Y. (2014). Effect of plate-like alumina on the properties of alumina ceramics prepared by gel-casting. Mater. Sci. Eng. 589, 97–100. https://doi.org/ 10.1016/j.msea.2013.09.061.
- 43. Ritchie, R.O. (2011). The conflicts between strength and toughness. Nat. Mater. 10, 817–822. https://doi.org/10.1038/nmat3115.
- Pham, M.S., Liu, C., Todd, I., and Lertthanasarn, J. (2019). Damage-tolerant architected materials inspired by crystal microstructure. Nature 565, 305–311. https://doi.org/10.1038/ s41586-018-0850-3.
- Chen, D., and Zheng, X. (2018). Multi-material Additive Manufacturing of Metamaterials with Giant, Tailorable Negative Poisson's Ratios. Sci. Rep. 8, 9139. https://doi.org/10.1038/ s41598-018-26980-7.
- Portela, C.M., Vidyasagar, A., Krödel, S., Weissenbach, T., Yee, D.W., Greer, J.R., and Kochmann, D.M. (2020). Extreme mechanical resilience of self-assembled nanolabyrinthine materials. Proc. Natl. Acad. Sci. USA 117, 5686– 5693. https://doi.org/10.1073/pnas. 1916817117.
- Therriault, D., Shepherd, R., White, S., and Lewis, J. (2005). Fugitive Inks for Direct-Write Assembly of Three-Dimensional Microvascular Networks. Adv. Mater. 17, 395–399. https://doi. org/10.1002/adma.200400481.
- 48. Kotz, F., Risch, P., Arnold, K., Sevim, S., Puigmartí-Luis, J., Quick, A., Thiel, M., Hrynevich, A., Dalton, P.D., Helmer, D., and Rapp, B.E. (2019). Fabrication of arbitrary threedimensional suspended hollow microstructures in transparent fused silica glass. Nat. Commun. 10, 1439. https://doi.org/ 10.1038/s41467-019-09497-z.
- Smith, R.L., Mecholsky, J.J., and Freiman, S.W. (2009). Estimation of fracture energy from the work of fracture and fracture surface area: I. Stable crack growth. Int. J. Fract. 156, 97–102. https://doi.org/10.1007/s10704-009-9350-7.
- Auerkari, P. (1996). Mechanical and Physical Properties of Engineering Alumina Ceramics (Technical Research Centre of Finland Espoo).
- Fukuhara, M., and Sanpei, A. (1993). Elastic moduli and internal friction of low carbon and stainless steels as a function of temperature. ISIJ Int. 33, 508–512.